Synthesis, structures and magnetic properties of $n=3$ Ruddlesden–Popper compounds $Ca_4Mn_{3-x}Ta_xO_{10}$ ($0 \leq x \leq 0.3$)

Ping Chai [a,b], Xiaojuan Liu [a], Yao Liu [a,b], Minfeng Lv [a], Jian Meng [a,*]

[a] State Key Laboratory of Rare Earth Resources Utilization, Changchun Institute of Applied Chemistry, Chinese Academy of Sciences, Changchun 130022, People's Republic of China
[b] Graduate School, Chinese Academy of Sciences, Beijing 100049, People's Republic of China

A R T I C L E   I N F O

A B S T R A C T

The structural and magnetic properties of Ta-doped $Ca_4Mn_{3-x}Ta_xO_{10}$ ($0 \leq x \leq 0.3$) compounds have been investigated. Structural refinement indicates that the Ta doping maintains the orthorhombic layered perovskite structure with space group *Pbca* as $Ca_4Mn_3O_{10}$ but induces an increase in both unit cell volume and octahedral distortion. The magnetization measurements reveal that the magnetization first increases and reaches to maximum for the $x=0.1$ sample and then gradually decreases with the increase of Ta content. There appear short-range ferromagnetic (FM) clusters in all the doped samples, which are caused by the double-exchange interaction between Mn^{4+} and Mn^{3+} that is induced by the charge compensation effect. As x is higher than 0.1, the overall results show evidence for the gradual appearance of a cluster glass behavior. When x increases to 0.3, the long-range antiferromagnetic (AFM) ground state is melted into the short-range magnetically ordered regions due to the increase of Ta^{5+} and Mn^{3+} at the expense of Mn^{4+}. The competition between AFM regions and FM clusters makes the short-range magnetic components frustrate when the temperature falls to a frustrating point, and thus cluster glass transition occurs.

© 2010 Published by Elsevier Inc.

1. Introduction

Due to their peculiar physical properties, perovskite manganites have attracted great attention with regard to scientific study and technological applications during the past decades [1]. With these materials, a ferromagnetic metal to a paramagnetic insulator transition takes place at a magnetic transition temperature T_c where colossal magnetoresistance (CMR) effect can be observed [2,3]. However, the functionality of perovskite manganites as industrial devices is often hindered by the high magnetic field and/or the low temperatures necessary to produce significant magnetoresistance. Recently, a great deal of research effort has extended into the Ruddlesden–Popper (RP) series of compounds in order to overcome these technological problems as well as to gain a greater insight into the various competing electronic interactions. The RP series, with general formula $(RA)_{n+1}Mn_nO_{3n+1}$ (R=rare earth; A=divalent alkaline metal), display a two-dimension character. Their crystal structure are composed of n layers of perovskite block alternating with a single layer of rock salt [4], which thus opens up new opportunities for tailoring the Mn–O interaction and tuning the resultant properties. It is well established that electron correlations are enhanced in two-dimensional materials. Therefore, for RP series of compounds with a lower dimensionality than that of the three-dimensional perovskite manganites, the magnetic and transport phenomena are expected to be interesting in terms of anisotropic structure and exchange interactions.

Among RP family, only the $n=2$ members have been widely investigated [5–7]. In particular, the single-crystal $La_{1.2}Sr_{1.8}Mn_2O_7$ shows an extremely large MR of 20000% that is much greater than that of the 3D perovskite manganites, revealing the importance of the effective dimensionality in CMR materials. To have a better understanding of the dimensionality effect on physical properties in the RP series, the investigation of other-layer members of RP compounds is highly desirable. Recently, several groups prepared the three-layer $Ca_4Mn_3O_{10}$ compound and investigated the crystal structure and physical properties. It has been found that the pure $Ca_4Mn_3O_{10}$, which is an antiferromagnetic insulator, exhibited rather weak CMR effect [8–11]. Witte et al. also investigated the electron-doped $Ca_{4-x}La_xMn_3O_{10}$ bulk compounds, but only slightly doping levels were available and thus no pronounced changes of property have been observed in the doped samples when comparing with $Ca_4Mn_3O_{10}$ [12]. Then many experimental studies directed towards the substitution of $Ca_4Mn_3O_{10}$ at Mn sites with pentavalent or hexavalent cations. Carvalho et al. successfully substituted Mn of $Ca_4Mn_3O_{10}$ by pentavalent V with the substitution ratio up to 10% and detected ferromagnetic behavior and CMR effect in this system [13]. Subsequently,

the highest substitution ratio of 10% of Mn by hexavalent Mo was also achieved in $Ca_4Mn_3O_{10}$. Meanwhile, the Mo substitution introduced an inhomogeneous magnetic ground state with ferromagnetic (FM) clusters embedded in an antiferromagnetic (AFM) matrix and obvious CMR effect was observed [14]. More recently, our group doped $Ca_4Mn_3O_{10}$ with pentavalent Nb at Mn sites [15], the observed properties of $Ca_4Mn_{3-x}Nb_xO_{10}$ showed a strong analogy to that of $Ca_4Mn_{3-x}V_xO_{10}$. It is clear that the substitution of $Ca_4Mn_3O_{10}$ at Mn sites with higher cations can show higher doping levels and thus induce mixed Mn^{3+}/Mn^{4+} and then interesting physical properties. However, up to date, besides the V^{5+}, Mo^{6+} and Nb^{5+} substitutions no other higher valent ion substitution of $Ca_4Mn_3O_{10}$ at Mn sites have been reported. Therefore, we performed the substitution of Mn by Ta in $Ca_4Mn_3O_{10}$ in order to obtain complete insight into this system. In this paper, we report on the detailed studies of the synthesis, structural and magnetic properties of the $Ca_4Mn_{3-x}Ta_xO_{10}$ ($0 \leq x \leq 0.3$).

2. Experimental

The polycrystalline samples of $Ca_4Mn_{3-x}Ta_xO_{10}$ ($x=0$, 0.05, 0.1, 0.2 and 0.3) were prepared by the conventional solid-state techniques. Well mixed stoichiometric amounts of the $CaCO_3$, Mn_2O_3 and Ta_2O_5 powders were calcined in air first at 800 °C for 24 h, then at 1020 °C for 30 h, and finally at 1220 °C for 60 h with an intermediate grinding for homogenization. The resultant product was ground, pelletized, and sintered at 1320 °C for 24 h, then furnace cooled to room temperature.

The samples were characterized by room-temperature X-ray powder diffraction (XRD) measurements (Rigaku D/Max 2500; Cu $K\alpha$ radiation, $\lambda=1.5406$ Å) for phase purity and crystal structure determinations. The XRD patterns were obtained between 5° and 110° in steps of 0.02° with a counting time of 2 s per step and analyzed by Rietveld refinements using the GSAS programs [16]. The background Rietveld refinement was fitted with a shifted Chebyschev polynomial function, and a pseudo-Voigt function was employed to model the peak shapes in all cases. The initial positional parameters were obtained from the data previously reported for $Ca_4Mn_3O_{10}$ [8]. An overall isotropic temperature factor for each sample was refined. The occupation factors were fixed by taking sample stoichiometry into account, assuming that the Ta cations were randomly distributed over the two Mn sites and that all of the oxygen sites were fully occupied. A preferred orientation correction and an absorption correction were included in the refinement.

Elemental analysis using the energy-dispersive X-ray (EDX) emission technique gave the stoichiometric composition within experimental errors. X-ray photoelectron spectroscopy (XPS) measurements were performed using an ESCALAB MKII spectrometer with an Al KR X-ray excitation source. Measurements of magnetization were carried out on a quantum design superconducting quantum interference device (SQUID)-based magnetic properties measurement system.

3. Results and discussion

The XPS data are first analysed in order to establish the real valence states of Mn and Ta ions. The Mn 2p core level spectra of all samples are shown in Fig. 1, in which the corresponding Mn $2p_{3/2}$ and Mn $2p_{1/2}$ peaks are indicated. For $Ca_4Mn_3O_{10}$, the Mn $2p_{3/2}$ peak shows the typical shape of Mn^{4+} compounds with a centered value of 642.8 eV, in good agreement with the literature data for MnO_2 [17]. For the doped samples, with the increase of Ta content,
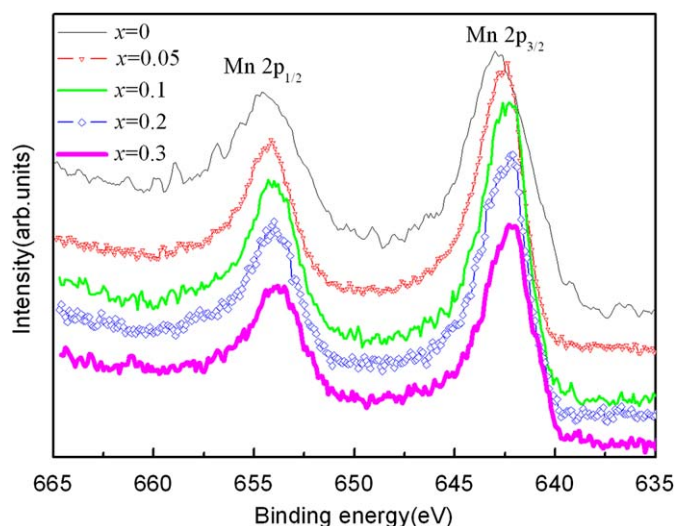

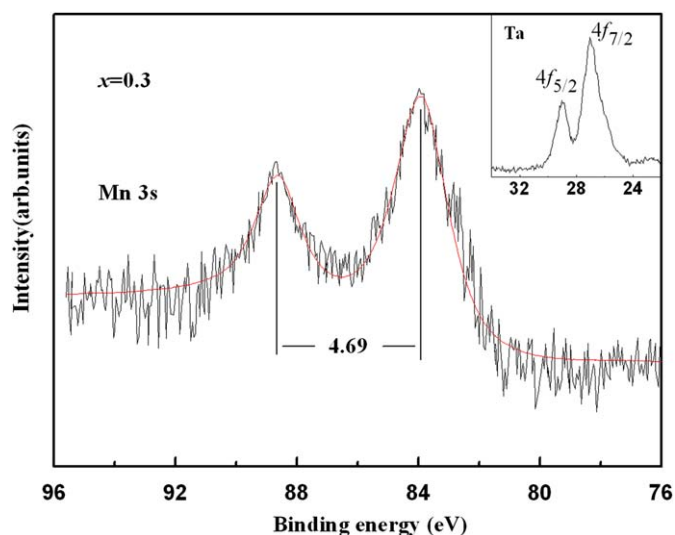**Fig. 1.** XPS spectra of Mn 2p region for $Ca_4Mn_{3-x}Ta_xO_{10}$.

Fig. 2. XPS spectra of Mn 3s and Ta 4f (inset) region for the selected $x=0.3$ sample.

the Mn $2p_{3/2}$ peak shifts gradually toward lower binding energy and reaches 642.0 eV for the $x=0.3$ sample. Noting that these values of Mn $2p_{3/2}$ peak are intermediate between those of Mn^{4+} and Mn^{3+} (641.5 eV in Mn_2O_3 [18]), it is clear that there appear some Mn^{3+}, i.e. the coexistence of Mn^{4+} and Mn^{3+} in the doped samples. It is well known that the 3s core level of the Mn ion exhibits the exchange splitting, which results from the exchange interaction between the Mn 3s and Mn 3d electrons, and the splitting magnitude depends on the valence state of the Mn ion [19]. Therefore, the core level spectra of Mn 3s were also measured in order to provide further evidence for the valence state of Mn ion. Fig. 2 shows the Mn 3s curve for selected $x=0.3$ sample and the corresponding fitting result is also given by solid line. As indicated, the splitting value of Mn 3s is around 4.69 eV. This value is intermediate between those of $SrMnO_3$ with Mn^{4+} and of $LaMnO_3$ with Mn^{3+} [20], confirming the coexistence of Mn^{4+} and Mn^{3+} in the doped samples. The XPS spectrum of Ta 4f for the selected $x=0.3$ sample is shown in the inset of Fig. 2. The binding energy of Ta $4f_{7/2}$ and $4f_{5/2}$ are 27.05 and 29 eV, respectively, which is consistent with that of the Ta_2O_5 [21], indicating that the Ta ion remained pentavalent. This result is also compatible with the fact

that the Ta^{5+} is most stable in the air. In summary, the XPS measurements indicate that the Ta^{5+} entered into the lattice and then induced Mn^{3+} in the Mn^{4+} matrix. This point is very important to the properties of the samples discussed below.

The room temperature powder X-ray diffraction spectra, analysed by Rietveld method, reveal that each of the samples is single phase of an orthorhombic layered perovskite structure with space group $Pbca$. The experimental, calculated, and difference X-ray diffraction patterns are shown in Fig. 3. It is clear that a good level of agreement between the observed and calculated patterns for all samples is obtained. The final atomic positions for $Ca_4Mn_{2.7}Ta_{0.3}O_{10}$ are given in Table 1. The refined structural parameters, agreement factors, and selected bond length and angles are listed in Table 2. The schematic crystal structure of $Ca_4Mn_3O_{10}$ is shown in Fig. 4.

Fig. 5 shows the evolution of the lattice parameters and cell volume with increasing Ta substitution in B-site. It is clear that the substitution causes an increase of a and b parameters but small irregular variation of c parameter with an overall increase of the cell volume. The increase of cell volume can be explained by the larger ionic radii of both Ta^{5+} and Mn^{3+}, generated in Mn^{4+} matrix (ionic radii of Ta^{5+}, Mn^{3+}, and Mn^{4+} are 0.64, 0.645, and 0.53 Å, respectively.). The spontaneous orthorhombic strain, defined as $s = 2(a+b)/(a-b)$, which is a measure of the distortion of the octahedron [22], is calculated. As listed in Table 2, the s value shows a rise as x increasing, revealing that the octahedral distortion progressively increases. This is in good agreement with the increase in the amount of Mn^{3+} that can lead to Jahn–Teller distortion of the octahedra.

The dependence of the average Mn–O bond length ($\langle Mn-O \rangle$) on the Ta content is shown in Fig. 6. It is clear that the $\langle Mn-O \rangle$ increases with Ta doping, consistent with the appearance of larger ion of Ta^{5+} and Mn^{3+} in Mn^{4+} matrix. As for the octahedra in the central of the perovskite blocks of $Ca_4Mn_{3-x}Ta_xO_{10}$, the mismatch between the Mn(1)–O(1) and Mn(1)–O(5) bond lengths becomes more pronounced with Ta content increasing. This also occurs between the Mn(2)–O(k) (k=1–4) bond lengths in the case of the octahedra on the edges of the blocks. We employ the parameter Δ_d, concerning the deviation of Mn–O distances with respect to the average $\langle Mn-O \rangle$ value, defined as $\Delta_d = \sum_{n=1}^{6} [(d_n - \langle d \rangle)/\langle d \rangle]^2/6$,

to quantify the relative distortion of the MnO_6 octahedra [22]. As shown in Table 2, both the $\Delta_d(1)$ and $\Delta_d(2)$ values show significant increase as x increases, indicating the enhancement of the distortion for both the Mn(1)O_6 and Mn(2)O_6 octahedra. This result is compatible with the increase in the Jahn–Teller Mn^{3+} ion. As for each compound, the $\Delta_d(1)$ is smaller than $\Delta_d(2)$ and the axial O–Mn(1)–O bond angle is closer to 180° than the axial O–Mn(2)–O bond angle, demonstrating that the Mn(1)O_6 octahedra are more regular than the Mn(2)O_6 octahedra, in agreement with the previous report on $Ca_4Mn_3O_{10}$ [8,23]. The average bond angle $\langle Mn-O-Mn \rangle$ slightly decreases from $\sim$160.0 to $\sim$152.0 as x varies from 0 to 0.3, as shown in Fig. 6. This reflects the enhanced octahedral tilting with Ta doping.

The zero-field-cooled (ZFC) and field-cooled (FC) temperature dependences of the dc magnetizations for all samples, measured under an applied field of 1000 Oe, are shown in Fig. 7. For $Ca_4Mn_3O_{10}$, the ZFC curve shows a cusp at 115 K, where FC curve exhibits a big increase with temperature decreasing. These features are in qualitative agreement with the previous neutron-scattering studies [8], indicating a typical G-type antiferromagnetic (AFM) behavior with a small canted spin. For the $x=0.05$ and 0.1 samples, with temperature decreasing both the ZFC and FC curves exhibit a sharp rise at a transition temperature T_m, and below which the magnetizations are significantly enhanced as compared to $Ca_4Mn_3O_{10}$. These characterizations reveal a paramagnetism (PM) to ferromagnetism (FM)-like transition, suggesting the appearance

Table 1
Atomic positions for the selected $x=0.3$ compound.

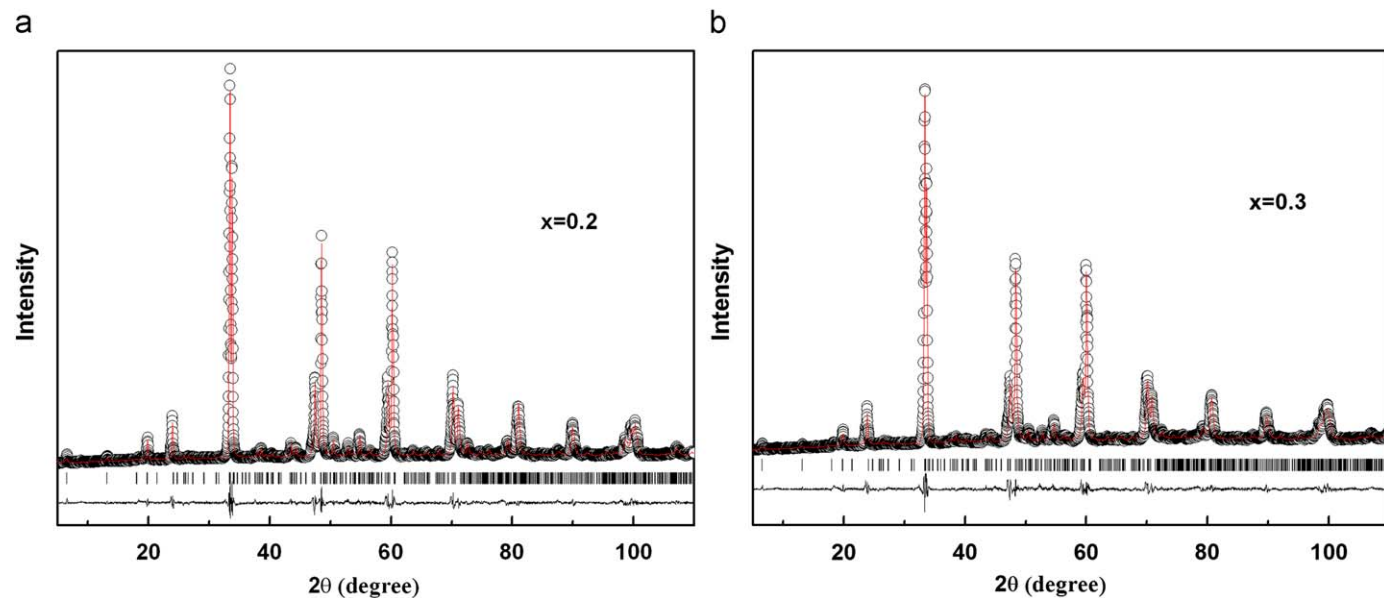| Atom	Site	x	y	z
Ca(1)	8c	0.5122(16)	0.5348(13)	0.06822(24)
Ca(2)	8c	0.0063(21)	0.0045(21)	0.20737(19)
Mn/Ta(1)	4b	0	0.5	0
Mn/Ta(2)	8c	0.5032(13)	−0.0016(12)	0.14066(10)
O(1)	8c	0.500(6)	0.0459(29)	0.0643(7)
O(2)	8c	0.545(4)	0.0498(29)	0.2107(7)
O(3)	8c	0.687(4)	0.309(5)	0.1215(8)
O(4)	8c	0.265(6)	0.770(6)	0.1467(7)
O(5)	8c	0.225(6)	0.228(6)	−0.0098(7)

Fig. 3. Observed (circles) and calculated (solid lines) Rietveld refinement plots of the XRD patterns for the selected (a) $x=0.2$ and (b) $x=0.3$ samples. The difference between observed and calculated is shown at the bottom of each pattern. Vertical tick marks represent allowed reflections.

Table 2
Results of the Rietveld refinement: unit cell parameters and volumes, selected Mn–O bond lengths (Å) and Mn–O–Mn angles (deg.), and reliability factors for $Ca_4Mn_{3-x}Ta_xO_{10}$ ($x=0$, 0.05, 0.1, 0.2 and 0.3) samples, space group $Pbca$, from RT XRD.

	$x=0$	$x=0.05$	$x=0.1$	$x=0.2$	$x=0.3$
a (Å)	5.26497(11)	5.27661(14)	5.28641(13)	5.30530(7)	5.32546(16)
b (Å)	5.26136(12)	5.27263(14)	5.28222(12)	5.30084(6)	5.32051(8)
c (Å)	26.8171(3)	26.8208(5)	26.8156(4)	26.8284(5)	26.8228(7)
V (Å^3)	742.858	746.198	748.798	754.483	760.002
$10^4 \times s^a$	3.43	3.77	3.96	4.21	4.65
Mn(1)–O(1) × 2	1.901(8)	1.899(9)	1.903(11)	1.889(14)	1.895(18)
Mn(1)–O(5) × 2	1.91(2)	1.923(29)	1.95(4)	1.977(21)	2.007(13)
Mn(1)–O(5) × 2	1.88(2)	1.887(29)	1.876(14)	1.882(21)	1.90(4)
⟨Mn(1)–O⟩	1.90(2)	1.903(22)	1.91(2)	1.916(19)	1.934(24)
$10^5 \times \Delta_d[Mn(1)O_6]^b$	4.63	6.18	25.63	50.90	71.35
Mn(2)–O(1)	1.923(8)	1.943(10)	1.985(19)	2.004(13)	2.020(12)
Mn(2)–O(2)	1.914(7)	1.903(9)	1.913(19)	1.906(15)	1.916(13)
Mn(2)–O(3)	1.91(2)	1.978(22)	1.982(17)	1.993(20)	1.997(27)
Mn(2)–O(3)	1.88(2)	1.853(23)	1.848(17)	1.908(23)	1.961(24)
Mn(2)–O(4)	1.92(2)	1.895(24)	1.910(18)	1.880(22)	1.909(30)
Mn(2)–O(4)	1.87(2)	1.889(24)	1.877(19)	1.859(23)	1.831(31)
⟨Mn(2)–O⟩	1.90(2)	1.910(19)	1.919(18)	1.925(19)	1.939(22)
$10^5 \times \Delta_d[Mn(2)O_6]^b$	11.66	44.2	69.0	82.3	104.2
⟨Mn–O⟩	1.90(2)	1.907(21)	1.915(19)	1.921(19)	1.937(23)
O(1)–Mn(1)–O(1)	180.0(0)	179.972(0)	179.980(0)	179.980(0)	180.000(0)
O(1)–Mn(2)–O(2)	175.4(6)	172.9(10)	175.1(8)	175.5(9)	163.5(8)
Mn(1)–O(1)–Mn(2) × 2	162.4(6)	167.0(11)	146.0(8)	155.7(7)	156.0(11)
Mn(1)–O(5)–Mn(1) × 4	154.7(6)	149.5(9)	149.3(8)	158.0(10)	155.282(0)
Mn(2)–O(3)–Mn(2) × 2	162.7(9)	159.3(9)	164.2(10)	128.7(10)	133.4(13)
Mn(2)–O(4)–Mn(2) × 2	158.5(8)	160.0(10)	161.5(10)	161.6(12)	160.1(12)
⟨Mn–O–Mn⟩	160.0(6)	157.1(4)	154.1(4)	152.4(3)	152.0(2)
χ^2	1.372	1.442	1.431	1.096	1.210
R_p(%)	8.11	8.12	7.49	5.61	5.35
R_{wp}(%)	10.55	10.41	9.62	7.51	7.20

[a] s is the spontaneous orthorhombic strain, defined as $s=2(a+b)/(a-b)$.
[b] Δ_d is a parameter indicating the relative distortion of the MnO_6 octahedra, defined as $\Delta_d = \sum_{n=1}^{6}[(d_n-\langle d\rangle)/\langle d\rangle]^2/6$.
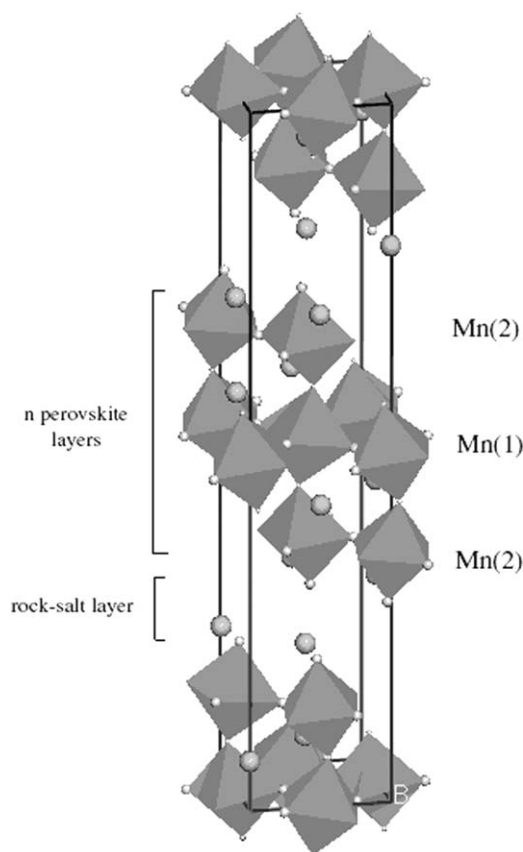

Fig. 4. Schematic crystal structure of $Ca_4Mn_3O_{10}$.

of a short-range ferromagnetic (FM) coupling and the formation of FM clusters in these doped samples [13–15]. Moreover, there appears irreversibility between ZFC and FC magnetizations at a temperature T_r just below T_m and the magnetization cannot reach saturation at low temperature, which is also the features of the inhomogeneous ferromagnetism. As for $x=0.2$ samples, besides the appearance of the PM–FM-like transition, the FC curve continues to increase strongly, while the ZFC curve increases gradually to its maximum around a temperature T_f ($T_f=17$ K) with lowering temperature. As x increases to 0.3, the ZFC curve shows a more pronounced maximum peak at 41 K. Note that the large difference between FC and ZFC magnetizations and the peak in ZFC curve are the typical experimental signature for several spin-glass-like states including spin glass, reentrant spin glass, and cluster glass [24]. We speculate a possible spin-glass-like transition occurring at 17 and 41 K for $x=0.2$ and 0.3 sample, respectively. In canonical spin glass system the FM magnetization shows a nearly constant value below the irreversibility temperature T_r, which is inconsistent with the present cases; in the reentrant spin glass system the irreversibility between ZFC and FC curves arises at a temperature well below T_m ($T_r \ll T_m$) but in cluster glass system T_r is just below T_m [25,26], which is observed in the case of present samples. Therefore, it can be obtained that the ground states for $x=0.2$ and 0.3 samples should be cluster glass. In fact, cluster glass state was observed in many similar systems, such as $Ca_4Mn_3O_{10}$ with Mo doping and $La_{2/3}Ca_{1/3}MnO_3$ with Ga, Al, and Fe doping at the Mn site [27–29]. Furthermore, notice that with the Ta content increasing, the magnetization continuously increases until x reaching to 0.1 and then gradually decreases and the transition temperature T_m presents a gradual decrease (see Table 3), which indicate that the Ta doping leads to the complex evolution of the magnetic structure.
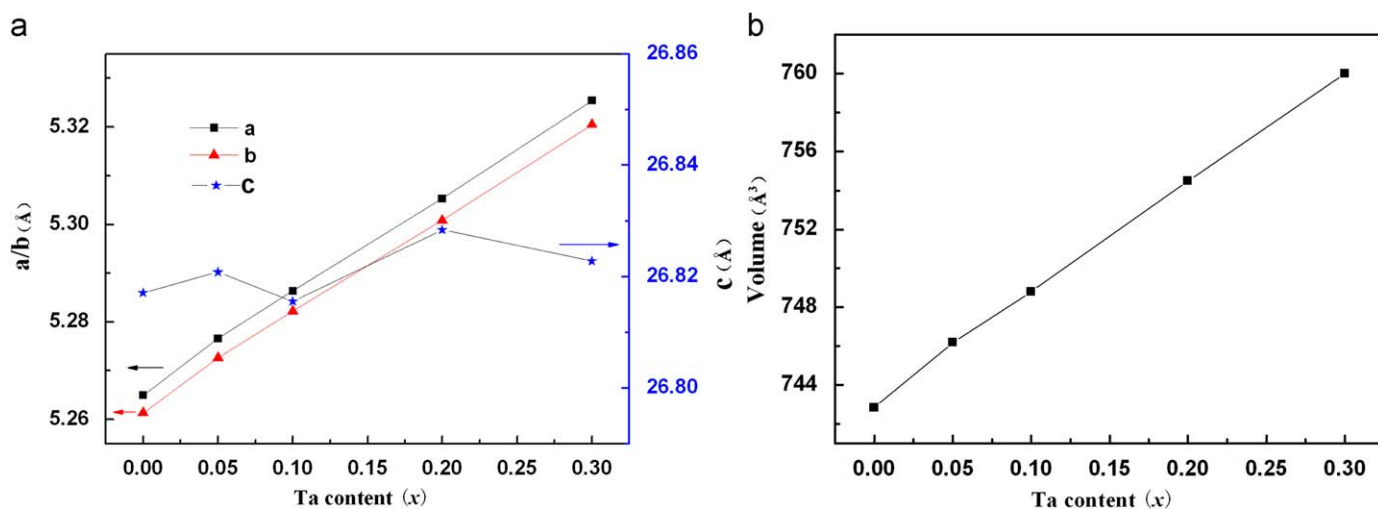
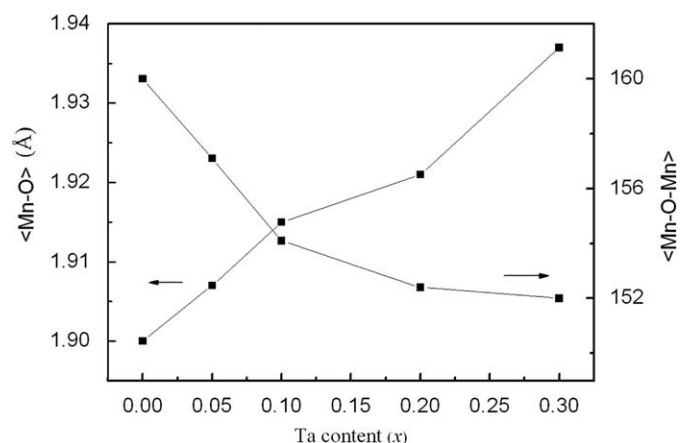**Fig. 5.** (a) Lattice parameters and (b) unit cell volume as a function of Ta content.

Fig. 6. Average Mn–O bond length ($\langle$Mn–O$\rangle$) and Mn–O–Mn bond angle ($\langle$Mn–O–Mn$\rangle$) as a function of Ta content.

The ac susceptibility measurement is a very efficient way to evidence glassy behavior, so we measured the ac magnetic susceptibility χ_{ac} as a function of T at H_{ac}=10 Oe and different frequencies (10, 100, and 1000 Hz) for the x=0.3 sample. The measured curves are shown in Fig. 8. Obviously, there is a peak around 41 K in the $\chi_{ac}-T$ curves and a frequency dependence can be observed. The peak shifts toward a higher temperature with increasing frequency, which confirms the spin-glass-like transition appearing at 41 K for the x=0.3 sample. However, the broad peak and the slight variation of the peak temperature with frequency are qualitatively different from the behavior of typical spin glass. Therefore, we can conclude that the x=0.3 sample exhibits the cluster glass behavior in the low temperature.

We replot the ZFC curves as $1/\chi-T$ relations shown in Fig. 9. Above the transition temperature the curves can be linearly fitted very well. The fitting parameters listed in Table 3 show that all of the Curie–Weiss temperature θ in the relation $\chi=C/(T-\theta)$ are negative, demonstrating that antiferromagnetic interaction remains dominant in all samples and the ferromagnetism displayed by the doped samples should result from short-range ferromagnetic clusters. From the fitted value of the Curie constant C, the effective magnetic moment is derived using the formula $C=N\mu_{eff}^2/3k_B$. As shown in Table 3, nearly all the obtained μ_{exp} is

larger than the corresponding theoretical paramagnetic moment μ_{cal} (given by $\mu_{calc}=g_J[S(S+1)]^{1/2}\mu_B$, orbital contribution quenched), which reveal that there exist some short-range magnetic interaction in high temperature PM region.

In order to further verify the magnetic property, the isothermal hysteresis loops for all samples were also measured. Fig. 10 shows the H dependence of magnetization M at T=5 K for all samples, measured through the field-increasing and field-decreasing cycles. For x=0 sample, M increases almost linearly with H, indicating the AFM nature. For x=0.05, 0.1 and 0.2, the magnetization shows a sharp rise at low magnetic field and then a linear increase with increasing field. This reveals a superposition of FM and AFM components. Meanwhile, the magnetic hysteresis becomes obvious with x increasing. As x increases to 0.3, the magnetization presents a slow increase with magnetic field increasing. Furthermore, the magnetic hysteresis becomes more remarkable and the coercive force H_C enlarges significantly. The significant enlargement of H_C is due to the large blocking of the domain wall motion, which indicates the large magnetic inhomogeneity state of the x=0.3 sample. Note that the magnetization is maximum for x=0.1 sample, which reveals the strongest ferromagnetism in the x=0.1 sample. It is well known that the high spin Mn gives spin-ordered moment $\mu=gs\mu_B$ where Mn^{3+} and Mn^{4+} carry $4\mu_B$ and $3\mu_B$, respectively. If all the samples were in a FM state, the maximum spin-only ordered moment would be 9, 8.9, 8.8, 8.6, 8.4μ_B per formula unit for x=0, 0.05, 0.1, 0.2 and 0.3, respectively. In fact, the measured M at T=5 K and H=6 T is found to be 0.37, 0.80, 1.92, 0.96 and 0.58μ_B per formula unit, which is much smaller than the theoretical values, further indicating that the FM component is small in the samples. The inset of Fig. 10 shows only the virgin branches of the $M(H)$ curves for x=0.2 and 0.3 samples, in which there is no S shape can be observed. This phenomenon is inconsistent with the behavior of both canonical spin glass and reentrant spin glass [25,30], further confirming the cluster glass ground state of the x=0.2 and 0.3 samples.

Let us now summarize the magnetic results to reach a conclusion about the magnetic nature of the Ca$_4$Mn$_{3-x}$Ta$_x$O$_{10}$ (x=0, 0.05, 0.1, 0.2 and 0.3) samples. The undoped Ca$_4$Mn$_3$O$_{10}$, as reported in previous literature, exhibits a canted G-type AFM state. As Ta^{5+} is added, there appear short-range FM clusters in the samples. Namely, the doped samples consist of FM clusters and AFM components, and thus can be described by the phase separation picture. When x=0.2, the sample turns to a cluster
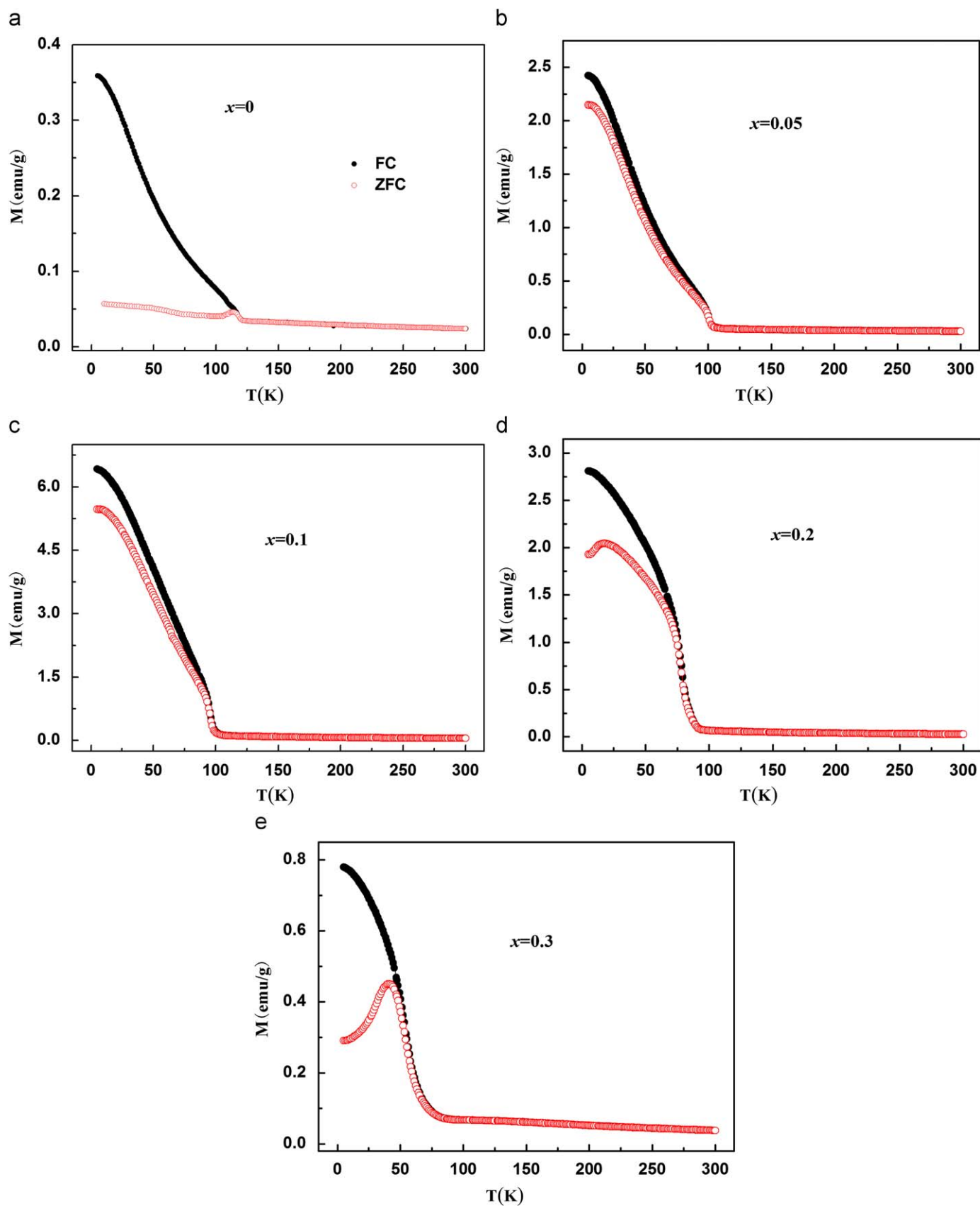
Fig. 7. Magnetization as a function of temperature measured under 1000 Oe for (a) x=0, (b) x=0.05, (c) x=0.1, (d) x=0.2, and (e) x=0.3 samples (ZFC curves, open symbols; FC curves, solid symbols).

Table 3
The PM–FM transition temperature T_m, Weiss temperatures θ and effective magnetic moments μ_{exp} obtained from the Curie–Weiss law, and the calculated effective magnetic moments μ_{calc}.

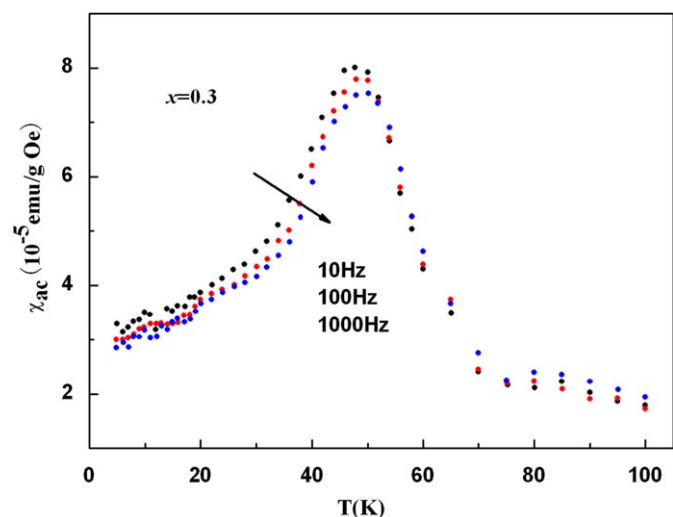| x	T_m (K)	θ (K)	μ_{exp} (μ_B)	μ_{calc} (μ_B)
0	115	−145	4.03	3.87
0.05	105	−135	4.05	3.89
0.1	98	−70	5.17	3.91
0.2	90	−43	3.66	3.94
0.3	70	−77	4.72	3.98

Fig. 8. Measured ac susceptibility χ_{ac} as a function of T at $H_{ac} = 10$ Oe and different frequencies (10, 100, and 1000 Hz) for the $x=0.3$ sample.
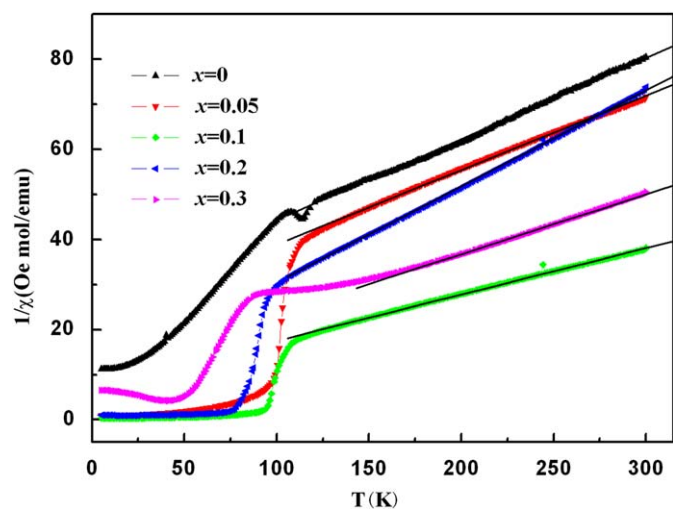

Fig. 9. The ZFC curves as $1/\chi - T$ relations with Curie–Weiss fits (solid lines).

glass behavior below 17 K. For $x=0.3$, the sample goes into a more pronounced cluster glass state below 41 K.

To understand the physics associated with Ta doping, we may first consider the charge compensation effect. The substitution with Ta induces the Mn^{3+} species with mobile electrons into the e_g band. As a result, the double-exchange (DE) interaction between Mn^{4+} and Mn^{3+} could be established, justifying the observed ferromagnetic clusters. Keeping this in mind, one may consider that the Ta doping can lead to the increase of the lattice sites participating in the itinerant DE interaction and thus the

ferromagnetism should increase gradually. However, this is not the case. In fact, as Ta^{5+} ion increases, besides the Mn^{3+} content increasing, many other effects also appear and should be considered simultaneously. First, as mentioned in the structural refinement section, the MnO_6 octahedral distortion becomes serious with Ta doping. Therefore, the overlap between the O $2p$ and Mn $3d$ orbital reduces, and then the ferromagnetic exchange coupling between Mn^{4+} and Mn^{3+} ions is weakened gradually with Ta doping. Second, the introduction of the nonmagnetic Ta^{5+} ion can enlarge the separation between the Mn ions, which then also weakens the ferromagnetic exchange coupling between Mn^{4+} and Mn^{3+} ions. Finally, the long-range AFM order between Mn^{4+} and Mn^{4+} ions is gradually broken with the Ta increasing. It is the competition among these effects that results in a complex evolution of magnetic structure with Ta content increasing. For the smaller doping samples, the Mn^{3+} is sparsely distributed in the Mn^{4+} matrix, forming small ferromagnetic clusters, which expand at the expense of Mn^{4+}–O–Mn^{4+} antiferromagnetic interaction as x increasing. Meanwhile, the MnO_6 octahedral distortion and the separation of Mn ions are weak. Therefore, the magnetization increases with x increasing from 0 to 0.1. However, due to the low doping level only short-range ferromagnetic clusters rather than long-range ferromagnetic ordering can be formed. With x further increasing to 0.2, both the MnO_6 octahedral distortion and the separation of Mn ions strengthen, although the number of FM cluster increases, the FM coupling interaction weakens. As a result, the magnetization starts to decrease. Up to $x=0.3$, the long-range AFM ground state is seriously disturbed so that it is melted into the short-range magnetically ordered regions. Consequently, AFM regions and FM clusters compete so strongly that lead to frustrate when the temperature falls to a frustrating point at which these short-range components begin to freeze due to the intercluster frustration. The cluster glass transition is thus activated. It is worth noting that the $x=0.2$ sample is in the intermediate state, where the FM interaction is moderate and the long-range AFM ground state is a little disturbed, which thus lead to the cluster-glass transition at lower temperature. Note that during the whole doping process, the ferromagnetic exchange coupling between Mn^{4+} and Mn^{3+} becomes weak gradually, which lead to the decrease in the transition temperature T_m with increasing Ta.

The evolution of the magnetic properties in present $Ca_4Mn_{3-x}Ta_xO_{10}$ system shows a strong analogy to that of previously reported $Ca_4Mn_{3-x}Mo_xO_{10}$ system [14]. Both Ta and Mo doping induce the FM clusters in the samples and then lead to the gradual appearance of cluster-glass state. However, there also exist differences between them. We compared the M–H curves in both series carefully. For $Ca_4Mn_{3-x}Ta_xO_{10}$, the $x=0.1$ sample shows the maximum ferromagnetism and its magnetization value reaches to $1.92\mu_B$ per formula unit at 5 K in applied field of 5 T; for $Ca_4Mn_{3-x}Mo_xO_{10}$, the maximum magnetization also appears in $x=0.1$ sample, but its value is only about $0.8\mu_B$ per formula unit at the same condition [14]. It is clear that the Ta doping has stronger ability to induce FM than Mo doping. This result is unexpected because the Mo and Ta ion are hexavalent and pentavalent, respectively, so the electron-doping rate is faster in $Ca_4Mn_{3-x}Mo_xO_{10}$ and thus the larger magnetization is expected for $Ca_4Mn_{3-x}Mo_xO_{10}$ system. Then we compared the magnetization of $Ca_4Mn_{3-x}Nb_xO_{10}$ system with $Ca_4Mn_{3-x}Ta_xO_{10}$ system. In $Ca_4Mn_{3-x}Nb_xO_{10}$ system, the maximum magnetization appears in $x=0.2$ sample and its value is about $0.8\mu_B$ per formula unit at 5 K in applied field of 5 T [15], which is much smaller than that of $Ca_4Mn_{3-x}Ta_xO_{10}$. Considering that Ta^{5+} ion possess the same inactive d^0 electronic configuration and the same size (0.64 Å) with Nb^{5+}, it is not clear why the FM are significantly larger in the $Ca_4Mn_{3-x}Ta_xO_{10}$ system. One may consider that the different
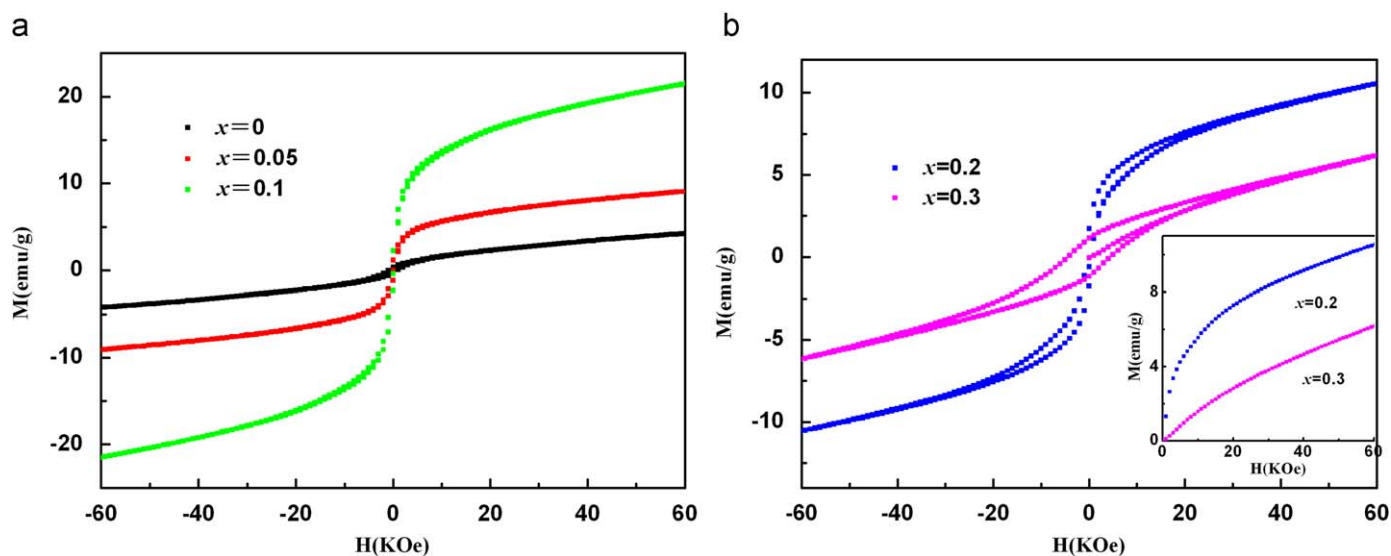
Fig. 10. The dc magnetization as a function of field measured at 5 K for (a) $x=0$, 0.05, 0.1, and (b) $x=0.2$, $x=0.3$ samples.

oxygen defects would lead to the different ferromagnetism in two systems. We have to stress that the synthesis routes are very close among these systems so that such large difference in FM should not be produced by only oxygen defects. These results indicate the speciality of Ta doping. The further understanding of the speciality of Ta^{5+} ion is in progress.

4. Conclusions

In conclusion, a series of $Ca_4Mn_{3-x}Ta_xO_{10}$ ($0 \leq x \leq 0.3$) compounds have been successfully prepared and investigated. The Ta doping in $Ca_4Mn_3O_{10}$ results in the following effects: (i) the coexistence of Mn^{4+} and Mn^{3+} induced by the charge compensation effect; (ii) unit cell volume, average Mn–O bond length and octahedral distortion of the samples increase progressively; (iii) the ferromagnetic transition temperature decreases but the magnetization shows a rise up to the $x=0.1$ sample and then gradually decreases; (iv) the short-range FM clusters appear in the doped samples; as x increase to 0.2 and 0.3, both samples exhibits cluster glass behavior at low temperature. With the increase of Ta content, the number of FM clusters increases, the FM interaction weakens, and the long-range AFM is disturbed gradually. The competition between these effects results in the gradual appearance of the cluster glass state. Furthermore, as compared to other related systems with higher valent cation substitution in B-site of $Ca_4Mn_3O_{10}$, Ta doping exhibits its speciality that the magnetization is significantly large.

References

[1] C.N.R. Rao, A.K. Cheetham, R. Mahesh, Chem. Mater. 8 (1996) 2421–2432.
[2] S. Jin, H.M. O'bryan, T.H. Tiefel, M. McCormack, W.W. Rhodes, Appl. Phys. Lett. 66 (1995) 382–385.
[3] P. Schiffer, A.P. Ramirez, W. Bao, S.W. Cheong, Phys. Rev. Lett. 75 (1995) 3336–3339.
[4] S.N. Ruddlesden, P. Popper, Acta Crystallogr. 11 (1958) 541–545.
[5] Y. Moritomo, A. Asamitsu, H. Kuwahara, Y. Tokura, Nature 380 (1996) 141–144.
[6] T. Kimura, A. Asamitsu, Y. Tomioka, Y. Tokura, Phys. Rev. Lett. 79 (1997) 3720–3723.
[7] A. Maignan, C. Martin, G. Van Tendeloo, M. Hervieu, B. Raveau, J. Mater. Chem. 8 (1998) 2411–2415.
[8] P.D. Battle, M.A. Green, J. Lago, J.E. Miillburn, M.J. Rosseinsky, J.F. Vente, Chem. Mater. 10 (1998) 658–664.
[9] J. Lago, P.D. Battle, M.J. Rosseinsky, A.I. Coldea, J. Singleton, J. Phys.: Condens. Matter 15 (2003) 6817–6833.
[10] R.C. Yu, S.Y. Li, J.L. Zhu, F.Y. Li, Z. Zang, C.Q. Jin, I.G. Voigt-Martin, J. Appl. Phys. 90 (2001) 6302–6305.
[11] J. Lago, P.D. Battle, M.J. Rosseinsky, J. Phys.: Condens. Matter 12 (2000) 2505–2524.
[12] N.S. Witte, P. Goodman, F.J. Lincoln, R.H. March, S.J. Kennedy, Appl. Phys. Lett. 72 (1998) 853–855.
[13] M.D. Carvalho, R.P. Borges, A.V. Girão, M.M. Cruz, M.E. Melo Jorge, G. Bonfait, P. Dluzewski, M. Godinho, Chem. Mater. 17 (2005) 4852–4857.
[14] W.J. Lu, Y.P. Sun, R. Ang, X. B Zhu, W.H. Song, Phys. Rev. B 75 (2007) 014414-1–014414-7.
[15] P. Chai, X.J. Liu, M.F. Lu, Z.L. Wang, J. Meng, Chem. Mater. 20 (2008) 1988–1996.
[16] A.C. Larson, R.B. von Dreele, General Structure Analysis System (GSAS); Report LAUR 86–748; Los Alamos National Laboratory: Los Alamos, NM, 1990.
[17] R.O. Ansell, T. Dickinson, A.F. Povey, Corros. Sci. 18 (1978) 245–248.
[18] B.N. Ivanov-Emin, N.A. Nevskaya, B.E. Zaitsev, T.M. Ivanova, Zh. Neorg. Khim. 27 (1982) 3101–3106.
[19] G.T. Tan, P. Duan, S.Y. Dai, Y.L. Zhou, H.B. Lu, Z.H. Chen, J. Appl. Phys. 93 (2003) 9920–9923.
[20] A. Kowalczyk, A. Ślebarski, A. Szajek, J. Baszyński, A. Winiarski, J. Magn. Magn. Mater. 212 (2000) 107–111.
[21] E. Atanassova, D. Spassov, A. Paskaleva, K. Kostov, Appl. Surf. Sci. 253 (2006) 2841–2851.
[22] J.A. Alonso, M.J. Martinez-Lope, M.T. Casais, Inorg. Chem. 39 (2000) 917–923.
[23] I.D. Fawcett, J.E. Sunstrom, M. Greenblatt, M. Croft, K.V. Ramanujachary, Chem. Mater. 10 (1998) 3643–3651.
[24] B. Roy, S. Das, J. Appl. Phys. 104 (2008) 103915-1–103915-11.
[25] R.S. Freitas, L. Ghivelder, Phys. Rev. B 64 (2001) 144404-1–144404-6.
[26] B. Roy, A. Poddar, S. Das, J. Appl. Phys. 100 (2006) 104318-1–104318-10.
[27] J.M. De Teresa, P.A. Algarabel, C. Ritter, J. Blasco, M.R. Ibarra, L. Morellon, J.I. Espeso, J.C. Gomez-Sal, Phys.Rev. Lett. 94 (2005) 20205–207208.
[28] J. Blasco, J. Garcia, J.M. DeTeresa, M.R. Ibarra, J. Perez, P.A. Algarabel, C. Marquina, C. Ritter, Phys. Rev. B 55 (1997) 8905–8910.
[29] J.W. Cai, C. Wang, B.G. Shen, J.G. Zhan, W.S. Zhan, Appl. Phys. Lett. 71 (1997) 1727–1730.
[30] X.H. Huang, J.F. Ding, G.Q. Zhang, Y. Hou, Y.P. Yao, X.G. Li, Phys. Rev. B 78 (2008) 224408-1–224408-5.